

Accelerating Targeted Hard-Label Adversarial Attacks in Low-Query Black-Box Settings

Arjhun Swaminathan*†‡

University of Tübingen, Germany

arjhun.swaminathan@uni-tuebingen.de

Mete Akgün†‡

University of Tübingen, Germany

mete.akguen@uni-tuebingen.de

Abstract—Deep neural networks for image classification remain vulnerable to adversarial examples — small, imperceptible perturbations that induce misclassifications. In black-box settings, where only the final prediction is accessible, crafting targeted attacks that aim to misclassify into a specific target class is particularly challenging due to narrow decision regions. Current state-of-the-art methods often exploit the geometric properties of the decision boundary separating a source image and a target image rather than incorporating information from the images themselves. In contrast, we propose Targeted Edge-informed Attack (TEA), a novel attack that utilizes edge information from the target image to carefully perturb it, thereby producing an adversarial image that is closer to the source image while still achieving the desired target classification. Our approach consistently outperforms current state-of-the-art methods across different models in low query settings (nearly 70% fewer queries are used), a scenario especially relevant in real-world applications with limited queries and black-box access. Furthermore, by efficiently generating a suitable adversarial example, TEA provides an improved target initialization for established geometry-based attacks.

Index Terms—adversarial machine learning, black-box attacks, computer vision.

I. INTRODUCTION

Deep neural networks have achieved remarkable performance in image classification tasks, powering applications from autonomous systems [1], [2] to medical diagnostics [3], [4]. However, they have repeatedly been shown to be vulnerable to adversarial examples [5], [6]. These are small, often imperceptible perturbations to a correctly classified image that cause a misclassification. Although many of these attacks assume white-box access to a model’s internals, hard-label (decision-based) attacks offer a more challenging yet practical setting where only the top-1 predicted label is observed. This limited-feedback scenario commonly arises in commercial APIs [7]. In this realm, targeted attacks, which push the model’s prediction to a specific target class, are inherently more difficult since the decision regions corresponding to the specific target classes are usually narrower and more isolated.

In black-box settings, targeted hard-label attacks have become an active area of research, with several techniques proposed in the literature [8]–[12], with state-of-the-art methods

relying on the geometry of the decision boundary separating the source image from the target class. Geometry-informed attacks traverse in a lower-dimensional space and fall into two categories: *Boundary Tracing Attacks* and *Gradient Estimation Attacks*. Boundary Tracing Attacks ([13]–[16]) perform walks along the decision boundary while Gradient Estimation Attacks ([17]–[23]) perform the same walks but using information about the approximate tangent/normal to the decision boundary in a local neighborhood to their adversarial image. Although powerful for local refinement, both approaches tend to burn through queries when the source image lies far from a given adversarial image in a target class, wasting many queries before reaching a narrow region where local geometry can more effectively be leveraged.

Further, in practice, many real-world scenarios such as commercial pay-per-query APIs, impose severe constraints on the number of queries that can be made to a target model in a specified time. Often practical query limits may be on the order of a few hundred to fewer than a few thousand queries. Under these conditions, the limited feedback available makes it difficult to effectively use information about the local decision boundary geometry in the early stages of an attack. When the decision space is still wide, movement along restricted lower dimensional spaces leads to limited incremental progress, and gradient estimation methods often use queries in estimating local gradients by sampling predictions in a local neighborhood instead of moving. This raises a pressing need to develop methods that are efficient in the low-query regime. In a high query setting, this would also lead us to a good starting point to employ the geometry-informed methods since we arrive at a good adversarial point quickly and can use the geometry-informed information more effectively. To this end, we propose Targeted Edge-Informed Attack (TEA), a novel targeted adversarial attack designed for hard-label black-box scenarios within a restricted query budget. Rather than depending on the local properties of the decision boundary, TEA leverages the intrinsic features of the target image itself - specifically, the edge information obtained using Sobel filters [24] help identify prominent structural features in the target image. Edges encode high-magnitude spatial gradients that delineate object boundaries [24]. Research has shown that early layers fire on oriented edge filters [25], [26], and that shape/edge cues remain predictive even when textures are suppressed [27]. The core idea is to preserve these low-level features, while applying

*Corresponding author.

†Medical Data Privacy and Privacy-preserving Machine Learning (MDPPML), University of Tübingen, Germany.

‡Institute for Bioinformatics and Medical Informatics (IBMI), University of Tübingen, Germany.

perturbations to the non-edge regions of an image, allowing us to stay in the target class while pushing the adversarial image towards the source image. When our progress plateaus, evidenced by a series of consecutive queries that fail to achieve further reduction in distance while maintaining target class prediction, one can switch to current state-of-the-art geometry-informed methods for a local refinement procedure. Hence we make the following contributions:

TEA: We introduce an edge-informed perturbation strategy, enabling rapid progress toward the source image in the early stages of an adversarial attack when limited queries are available. TEA involves a two-step process: First, a global edge-informed search is performed, and then, edge-informed updates are applied to small patches using Gaussian weights.

Empirical validation under strict query budgets: We perform extensive evaluations on the ImageNet validation dataset [28] across four architectures (ResNet-50 [4], ResNet-101 [4], VGG16 [29], and ViT [30]) and an adversarially trained architecture (ResNet-50 [31]). Our attack consistently outperforms existing state-of-the-art hard-label methods, including HSJA, Adaptive History-driven Attack (AHA) [32], CGBA, and CGBA-H, under realistic query budgets (fewer than 1000 queries). To achieve a 60% reduction in distance from a target image to a source image, TEA required on average 251 queries across the four models - 70% fewer than AHA (the second fastest), which required 845 queries.

The rest of this paper is structured as follows. Section 2 reviews related work on targeted hard-label adversarial attacks. Section 3 describes our methodology, while Section 4 presents experimental results. Finally, Section 5 outlines directions for future research.

II. RELATED WORKS

Early work in the realm of targeted hard-label adversarial attacks consisted of seminal work: Boundary Attack (BA) [13], which proposed a method of traversing the decision boundary that separates an adversarial image from a source image. Building on this framework, BiasedBA [14] incorporated directional priors, such as perceptual and low-frequency biases, to restrict the search to more promising regions. BA with Output Diversification Strategy (BAODS) [22] integrates diverse gradient-like signals into the exploration process of BA, thereby strengthening the original method.

Following these foundational methods, Hybrid Attack (HA) [16] employed a combination of heuristic search strategies to balance global exploration and local refinement. Advancing toward more gradient-centric techniques, qFool [19] leverages the local flatness of decision boundaries to streamline the attack process. Meanwhile, HopSkipJumpAttack (HSJA) [17] locally approximates the normal to the decision boundary to “jump off” from it before progressing toward the source image. Complementarily, Tangent Attack exploits locally estimated tangents of the decision surface to steer the adversarial perturbation toward the source image. Addressing the challenges posed by high-dimensional input spaces, Query Efficient Boundary Attack (QEBA) [18] projects gradient

estimation into lower-dimensional subspaces, such as the frequency domain, thus significantly reducing the number of required queries.

Incorporating historical query information, Adaptive History-driven Attack (AHA) [32] adapts its search trajectory based on previous successes and failures, while Decision-based query Efficient Adversarial Attack based on boundary Learning (DEAL) [17] employs an evolutionary strategy that concentrates queries on promising regions of the input space. SurFree [15] demonstrated that using 2D planes and semicircular trajectories toward the source image was an effective strategy. This was based on the fact that under the assumption of a flat decision boundary, the point on the boundary that is closest to the source image is precisely where the semicircular trajectory intersects it. Building on this idea, Curvature-Aware Geometric black-box Attack (CGBA) and its variant that is more suited for targeted attacks - CGBA-H [21], use normal estimation at the decision boundary to select the traversal plane. To the best of our knowledge, CGBA-H serves as the current state of the art in decision-based targeted adversarial attacks.

III. METHODOLOGY

In this section, we formalize the hard-label attack setting and detail our attack, which drastically reduces early query cost, especially when the target image is far from the source image, and exists in a wider decision space. Once the adversarial image achieves a good distance and reaches a narrow decision space, one can use the image as an initialization and continue refining with existing geometric-based methods.

Problem Statement. We consider a hard-label image classifier modeled by

$$f : [0, 1]^{C \times H \times W} \rightarrow \mathbb{R}^K, \quad (1)$$

where C denotes the number of color channels, H and W are the image height and width, and the classifier distinguishes among K classes. For any query image x , we do not observe its continuous output (e.g., logits or probabilities) but only the predicted label index

$$\hat{y}(x) = \arg \max_{1 \leq k \leq K} [f(x)]_k. \quad (2)$$

Let x_s be a *source* image correctly classified as y_s . In a *targeted* attack, we start with a *target* image x_t (correctly classified as y_t). Our goal is to find an adversarial image x_{adv} that is as close as possible to x_s (in the ℓ_2 norm) while maintaining the target classification, i.e.,

$$x_{\text{adv}} = \arg \min_x \|x - x_s\|_2, \quad \text{subject to } \hat{y}(x) = y_t. \quad (3)$$

We propose a two-part procedure for perturbing the target image x_t to get closer to x_s while maintaining adversarial requirements. First, a *global* edge-informed search coarsely aligns major image regions. Second, a *patch-based* edge-informed search further perturbs local regions in our adversarial image. Note that neither step leverages local decision boundary geometry or gradient estimation, which are typically

beneficial only when the adversarial image lies near a narrow decision space and when movements towards the source image are unlikely to maintain classification. This approach avoids burning queries in a wider decision space.

A. Global Edge-Informed Search

The global perturbation step aims to coarsely align x_t towards x_s by modifying predominantly smooth, non-edge areas, thereby preserving crucial edge structures that help maintain target classification.

Soft Edge Mask. To this end, we detect edges in x_t using the Sobel operator [24], as depicted in Figure 1. A subsequent blurring operation yields a *soft edge mask* M_{edge} , where $M_{\text{edge}}(i, j) \in [0, 1]$ has values close to 1 at edge locations and gradually transitions to 0 in smoother regions. We describe this in Algorithm 1.

Algorithm 1 Soft Edge Mask

```

1: Inputs: Image  $x$ , edge thresholds  $\{T_\ell, T_h\}$ , Gaussian blur kernel
   size  $b$ , intensity factor  $\gamma$ , small constant  $\epsilon$ 
2: Output: Soft edge mask  $M_{\text{edge}}$ 
3:  $x^{\text{gray}} \leftarrow \text{GrayScale}(x)$ 
4:  $(s_x, s_y) \leftarrow (\text{Sobel}(x^{\text{gray}}, 0), \text{Sobel}(x^{\text{gray}}, 1))$ 
5:  $G \leftarrow (s_x^2 + s_y^2)^{1/2}$ 
6:  $G \leftarrow 255 \cdot (G / (\max_{i,j}(G) + \epsilon))$ 
7:  $\text{edge\_mask}(i, j) \leftarrow \begin{cases} 255, & \text{if } T_\ell \leq G(i, j) \leq T_h, \\ 0, & \text{otherwise} \end{cases}$ 
8:  $\text{blurred} \leftarrow \text{GaussianBlur}(\text{edge\_mask}, (b, b))$ 
9:  $\text{norm} \leftarrow \text{Normalize}(\text{blurred})$ 
10:  $M_{\text{edge}} \leftarrow \gamma \cdot \text{norm}$ 
11: return  $M_{\text{edge}}$ 

```

Global Interpolation. Starting from $x_0 = x_t$, we perform iterative updates

$$x_{k+1} \leftarrow x_k + \alpha(x_s - x_k) \odot (I - M_{\text{edge}}), \quad (4)$$

where \odot denotes the element-wise (Hadamard) product. The scaling factor α is optimized via a momentum based search. Masking out the edge regions in this update ensures that the interpolation primarily affects smooth areas, thus preserving the overall structure necessary for target classification. The complete procedure is summarized in Algorithm 2. Once the improvements begin to stagnate, we transition to a local, patch-based refinement.

B. Patch-Based Edge-Informed Search

After the global interpolation, some subregions of the image may still display significant discrepancies from x_s . In the patch-based refinement, we then partition the image into randomly selected patches of random sizes

$$\mathcal{P} \subseteq \{1, \dots, H\} \times \{1, \dots, W\}, \quad (5)$$

and for each patch, construct a local soft edge mask $M_{\mathcal{P}}$ by restricting M_{edge} to \mathcal{P} . Next, starting from our adversarial image x_k , we apply a local interpolation

$$\tilde{x}(\beta) = x_k + \beta(x_s - x_k) \odot G \odot (I - M_{\mathcal{P}}), \quad (6)$$

Algorithm 2 Global Edge-Informed Search

```

1: Inputs: Source image  $x_s$ , target image  $x_t$ , soft edge mask
    $M_{\text{edge}}$ , tolerance  $\tau$ , maximum queries  $qc_{\text{max}}$ , initial step factor
    $\eta$ , momentum  $\mu$ 
2: Output: Adversarial image  $x_{\text{adv}}$  such that  $\hat{y}(x_{\text{adv}}) = y_t$ 
3:  $x_{\text{current}} \leftarrow x_t$ ,  $v \leftarrow 0$ , and  $d \leftarrow x_s - x_t$ 
4: Set step size:  $s \leftarrow \|d\|_2 \cdot \eta$ , and initialize query count  $qc \leftarrow 0$ 
5: while  $qc < qc_{\text{max}}$  and  $\|s\| \geq \tau$ 
6:    $v \leftarrow \mu \cdot v + (1 - \mu) \cdot d$ 
7:    $x_{\text{next}} \leftarrow x_{\text{current}} + s \cdot (v \odot (I - M_{\text{edge}}))$ 
8:    $qc \leftarrow qc + 1$ 
9:   if  $\hat{y}(x_{\text{next}}) = y_t$ 
10:     $x_{\text{current}} \leftarrow x_{\text{next}}$ 
11:     $s \leftarrow 1.1 \cdot s$ 
12:   else
13:     break
14: return  $x_{\text{current}}$ 

```

and search for the largest β such that the classifier still predicts the target label, $\hat{y}(\tilde{x}(\beta)) = y_t$. Here, G is a Gaussian weighting function over the patch that smoothly downweights updates near patch borders, helping to avoid artificial edges introduced by patch boundaries. We repeat this for different patches until a termination criterion is met (e.g., 25 consecutive iterations with no further improvement). The corresponding illustration is depicted in Figure 1 and the relevant pseudocode is provided in Algorithm 3.

Figure 2 offers a visual overview of TEA. The figure depicts the adversarial image throughout our method, and displays a hotspot of individual pixel differences from the source image.

IV. EXPERIMENTS

In this section, we present our empirical evaluation benchmarking *TEA* against existing targeted hard-label attacks. In what follows, we describe our experimental setup and metrics, then detail the performance of each method under a range of query budgets. Our findings indicate that *TEA* achieves efficient distance reduction to the source image, particularly in the early query regime, before switching to the current state-of-the-art geometry-based attack *CGBA-H* for further refinement in a narrow decision space.

A. Setup and Metrics

Computational Resources. The experiments were executed on a High-performance computing (HPC) Cluster. Each node on the cluster consisted of four NVIDIA GeForce GTX 1080 Ti GPUs (one GPU was allocated per source-target pair for a given attack).

Dataset and Image Pairs. We randomly sample 1000 source-target image pairs from the ImageNet ILSVRC2012 validation set, ensuring each pair contains images from distinct classes. All images are resized to $3 \times 224 \times 224$. Each pair (x_s, x_t) contains a source image x_s , correctly classified under its label, and a target image x_t , also correctly classified under a different label. The goal is to modify x_t to approach x_s under the ℓ_2 norm while keeping the prediction unchanged.

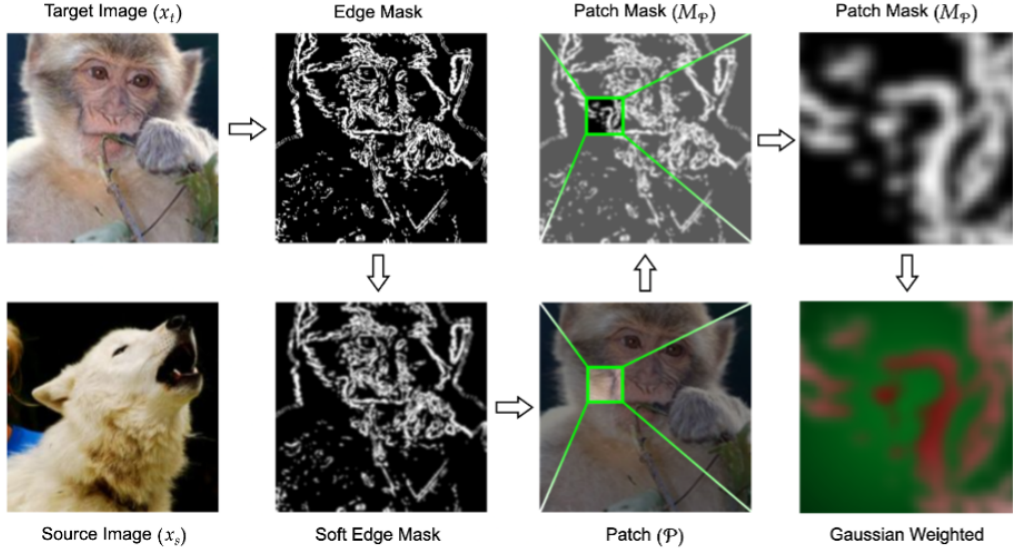


Fig. 1. **Overview of Patch-Based Edge-Informed Search.** Edge information from the target image, obtained via the Sobel operator, is first blurred to generate a soft edge mask. A square patch is then selected and a Gaussian weighting function is applied. In the bottom right panel, the intensity of the modification is illustrated: dark red regions remain largely unchanged, while light green regions receive a more pronounced update. The lack of changes near the patch borders helps prevent the introduction of artificial edges.

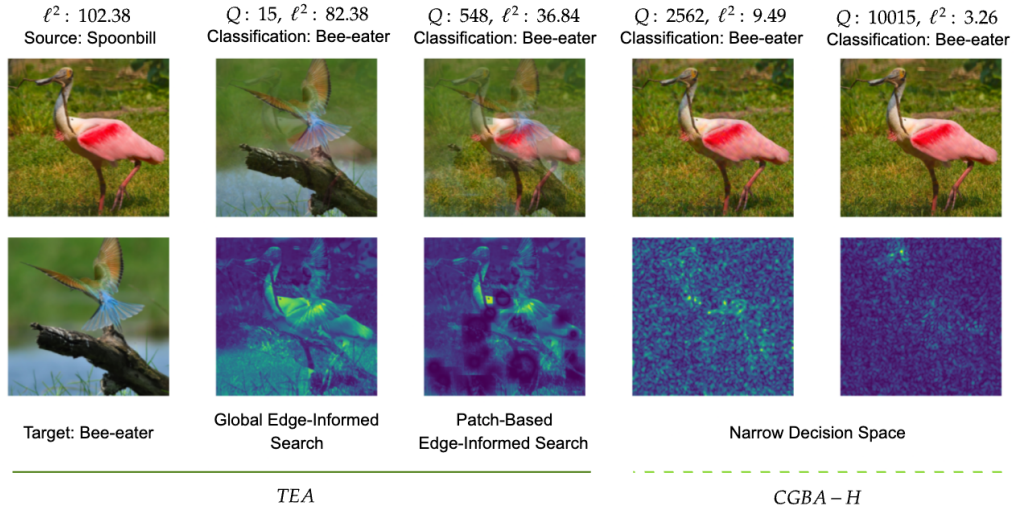


Fig. 2. **Visualization of TEA on a source–target image pair.** The target image (initially classified as *Bee-eater*) is perturbed to resemble the source image (classified as *Spoonbill*), while preserving its original *Bee-eater* label. Global Edge-Informed Search efficiently applies edge-aware perturbations using only 15 queries to achieve a $\approx 20\%$ reduction in distance to the source. Patch-Based Edge-Informed Search introduces localized, edge-aware modifications to small image regions, as seen in the hotspot of changes. Further refinement utilizing CGBA-H is illustrated in the narrow decision space.

Target Models. We evaluate our approach on four well-known classifiers: ResNet50 and ResNet101 (CNNs of varying depth), VGG16 (a CNN composed of repeated convolutional blocks), and ViT (a vision transformer that processes images as sequences of patches). These models represent a diverse set of architectures.

Compared Methods. We compare our method to four targeted hard-label attacks: HSJA, AHA, CGBA, and CGBA-H. For each method, the ℓ_2 distance to the source image is recorded after each set of queries, and along with the classification label of the perturbed target image.

Evaluation Metrics. Performance is quantified using three metrics. First, we compute the ℓ_2 distance from x_s to the adversarial example generated for each of the 1000 image pairs as queries progress. Second, the attack success rate (ASR) is defined as the fraction of image pairs for which an $\alpha\%$ reduction in ℓ_2 distance between adversarial image and source image is achieved as compared to the target image and source image. Third, we also measure the performance of each method when there is a set fixed low-query budget by measuring the ASRs for all α when each method has used up 500 queries. Finally, we integrate the ℓ_2 distance versus

Algorithm 3 Patch-Based Edge-Informed Search

```

1: Inputs: Source image  $x_s$ , current adversarial image  $x_{\text{adv}}$ , soft
   edge mask  $M_{\text{edge}}$  (from create_soft_edge_mask), minimum
   patch size  $p_{\min}$ , maximum patch size  $p_{\max}$ , step factor  $\eta$ ,
   momentum  $\mu$ , maximum calls  $N_{\max}$ 
2: Output: Refined adversarial image  $x_{\text{adv}}$ 
3:  $n_{\text{break}} \leftarrow 0$ 
4: while  $n_{\text{break}} < 25$ 
5:    $D \leftarrow \text{AvgPool}(|x_s - x_{\text{adv}}|)$ 
6:   Select high-difference indices from  $D$  and choose a random
      center  $(i_c, j_c)$ 
7:    $p \leftarrow \text{randInt}(p_{\min}, p_{\max})$ ;  $\mathcal{P} \leftarrow \{(i, j) \mid |i - i_c| \leq$ 
       $|p/2|, |j - j_c| \leq |p/2|\}$ 
8:    $M_{\mathcal{P}}(i, j) \leftarrow \begin{cases} 1, & (i, j) \in \mathcal{P}, \\ 0, & \text{otherwise.} \end{cases}$ 
9:    $x_{\text{patch}} \leftarrow \text{Patch}(x_{\text{adv}}, \mathcal{P})$ 
10:   $m_{\text{patch}} \leftarrow 0$ ,  $d_{\text{base}} \leftarrow \|x_s - x_{\text{adv}}\|_2$ 
11:  for iteration = 1 to  $N_{\max}$ 
12:     $d_{\text{local}} \leftarrow \text{Patch}(x_s, \mathcal{P}) - x_{\text{patch}}$ 
13:     $m_{\text{patch}} \leftarrow \mu \cdot m_{\text{patch}} + (1 - \mu) \cdot d_{\text{local}}$ 
14:     $s_{\text{patch}} \leftarrow \eta \cdot \|x_s - x_{\text{adv}}\|_2$ 
15:     $G \leftarrow \text{GaussianWeight}((i_c, j_c), \sigma = p/3)$ 
16:     $\Delta x \leftarrow s_{\text{patch}} \cdot m_{\text{patch}} \odot (G \odot (1 - (M_{\text{edge}} \odot M_{\mathcal{P}})))$ 
17:     $x_{\text{patch}}^+ \leftarrow x_{\text{patch}} + \Delta x$ 
18:     $x_{\text{temp}} \leftarrow x_{\text{adv}} - x_{\text{adv}} \odot M_{\mathcal{P}} + x_{\text{patch}}^+ \odot M_{\mathcal{P}}$ 
19:     $d_{\text{new}} \leftarrow \|x_s - x_{\text{temp}}\|_2$ 
20:    if  $d_{\text{new}} \geq 0.999 \cdot d_{\text{base}}$ 
21:      break
22:    if  $\hat{y}(x_{\text{temp}}) = y_t$ 
23:       $x_{\text{patch}} \leftarrow x_{\text{patch}}^+$ 
24:       $x_{\text{adv}} \leftarrow \text{Replace}(x_{\text{adv}}, \mathcal{P}, x_{\text{patch}})$ 
25:       $d_{\text{base}} \leftarrow d_{\text{new}}$ 
26:       $n_{\text{break}} \leftarrow 0$ 
27:    else
28:       $n_{\text{break}} \leftarrow n_{\text{break}} + 1$ 
29:    break
30: return  $x_{\text{adv}}$ 

```

queries curve to obtain the area under the curve (AUC), which provides an aggregated measure of how rapidly the distance is reduced.

Implementation Details. Our implementation employs a two-stage process. In the first stage, we perform our proposed methodology TEA, where edge-aware distortions are applied to the target image while preserving its target classification, allowing a rapid reduction in distance to the source image. In the second stage, once the perturbations have brought the image into a narrow decision space, the method switches to CGBA-H for further refinement (denoted as TEA* throughout the study). The last query performed with TEA is referred to as the *turning point* throughout the study. We switch to CGBA-H since it consistently performs better than other methods in a high query setting across different architectures.

B. Results

Average ℓ_2 -Distance vs. Queries. Table I presents a comparative analysis of the median ℓ_2 distances achieved in the low-query regime—specifically, within the range defined by the average turning point computed over one thousand image pairs. This analysis underscores the rapid decrease in pertur-

bation norm facilitated by TEA during the early query stages. Figure 3 extends this evaluation by depicting the average percentage reduction in ℓ_2 distance against queries used. In the plots, the initial inflection point marks TEA’s transition from global exploration to patch-based refinement.

Attack Success Rate. In Figures 4 and 5, we show how many images reach at least 50% and 75% distance reduction over queries respectively. A sharper increase in this fraction signifies that more pairs experience substantial improvement more quickly. Again, once the turning point is reached between a pair, CGBA-H is implemented for further refinement.

Success at a Fixed Low-Query Budget. Figure 6 reports, at a low-query budget of 500 queries, the proportion of image pairs that reach or exceed various distance-reduction thresholds. TEA maintains a consistently higher proportion of successful pairs across nearly all thresholds, suggesting that its early-stage perturbations secure significant distance reductions more rapidly.

AUC Comparisons. We assess the efficiency of our approach by computing the area under the median ℓ_2 -distance vs queries curve (AUC). Table II presents the AUC values for the low-query regime, up to the turning point. Across all architectures, TEA consistently yields lower AUC values.

Evaluation on an Adversarially Trained Model. In Figure 7, we present a comparative analyses of performance against an adversarial trained model (Resnet50 from MardyLab [31]) in the low-query region. We see that TEA consistently achieves more distortion, while also noting that all methods perform significantly worse compared to the standard Resnet50 model as seen in Figure 3.

Edge Ablation Study To better understand the role of edge preservation in our method, we perform an ablation study by comparing three variants of TEA under identical settings. TEA perturbs non-edge pixels, preserving edge regions with a soft edge mask. INV-TEA inverts TEA’s soft edge mask to perturb primarily edge-like pixels. HALF-TEA perturbs non-edge and edge regions equally, using the same editable-pixel budget as TEA, and serves as a simple control baseline. Table III summarizes results in the low-query regime: median ℓ_2 distance, ASR at 50% distance reduction, and ASR at 75% distance reduction. Across all four architectures, TEA achieves the lowest median ℓ_2 and the highest success rates overall; HALF-TEA is consistently in between, and INV-TEA performs the worst, indicating that prioritizing non-edge regions proves crucial for early attack progress while preserving the semantic structure.

Randomness and Stability Across Patch Selection Our patch-based refinement uses random patch locations and sizes, introducing stochasticity. To quantify this effect, we executed five independent runs per model. For each run and query budget, we computed the average ℓ_2 distance across all pairs; we then summarized the five runs by reporting mean \pm standard deviation (std) of the average ℓ_2 distance across all pairs. As seen in Table IV, across all models and budgets, variability is small relative to the mean. The standard deviation is typically below 0.3 (well under 1% of the mean).

TABLE I
MEDIAN ℓ_2 DISTANCES COMPUTED UNTIL THE TURNING POINT ACROSS DIFFERENT ARCHITECTURES.
LOWER ℓ_2 VALUES DENOTE FASTER ADVERSARIAL EXAMPLE GENERATION.

Query	ResNet50					Query	ResNet101				
	HSJA	CGBA	CGBA-H	AHA	TEA		HSJA	CGBA	CGBA-H	AHA	TEA
100	92.797	88.857	83.104	80.438	75.2155	100	90.962	85.623	81.376	82.574	74.5036
200	88.715	87.165	79.348	75.344	62.0338	200	88.194	84.246	74.738	77.869	61.3794
300	88.604	86.236	74.168	71.054	55.5589	300	87.954	83.750	71.874	70.676	54.9321
400	88.199	85.579	71.479	67.091	51.9530	400	87.356	82.483	68.803	67.051	51.3780
500	87.724	84.897	68.671	64.172	49.8352	500	87.222	81.543	66.169	63.717	49.3863
602	87.203	83.937	66.774	61.168	45.6000	592	87.133	80.339	64.528	61.134	45.1390
Query	VGG16					Query	ViT				
	HSJA	CGBA	CGBA-H	AHA	TEA		HSJA	CGBA	CGBA-H	AHA	TEA
100	93.966	92.154	85.805	84.770	77.2608	100	80.454	76.885	73.074	68.863	67.5654
200	89.884	90.899	81.599	78.445	63.6530	200	79.981	74.702	69.511	65.501	56.1255
300	89.665	90.516	74.359	73.174	56.9954	300	79.606	74.139	63.655	63.951	50.8059
400	88.943	89.880	70.559	68.538	53.4018	400	79.599	72.839	61.300	59.857	47.8666
500	88.919	89.563	67.745	65.569	51.3763	500	78.761	71.291	58.598	56.572	46.2528
588	88.389	88.362	66.578	62.126	47.4840	554	78.626	69.954	57.710	54.494	43.4220

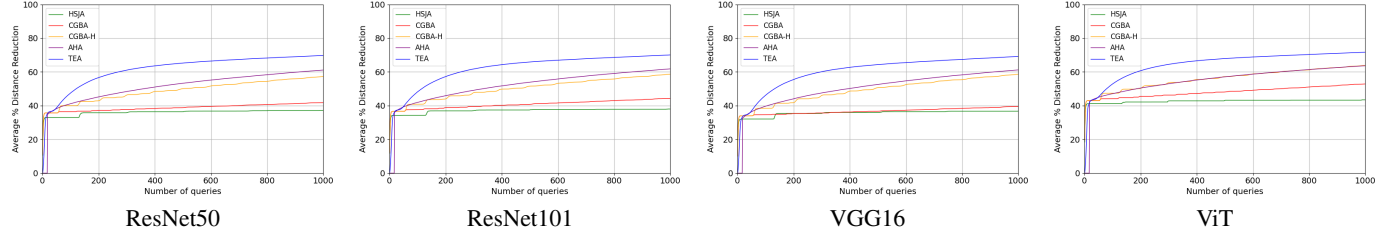


Fig. 3. Average ℓ_2 distance reduction across different architectures in a low-query regime. Higher values indicate improved performance.

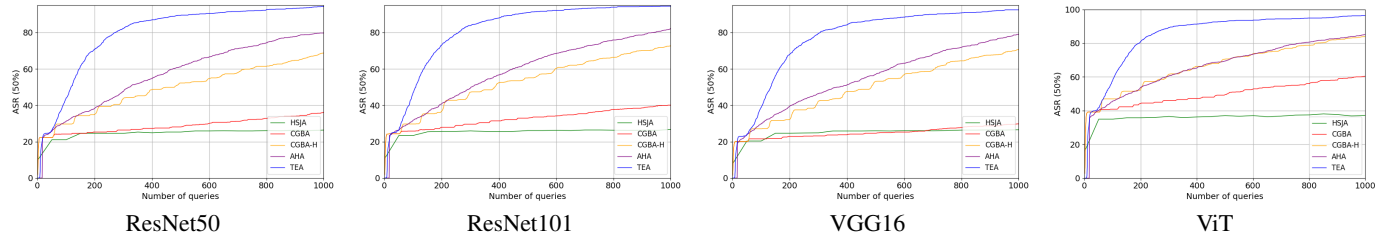


Fig. 4. Comparison of ASR of 50% distance reduction. Higher values indicate that a higher proportion of images reach a distance reduction of 50% sooner.

TABLE II
AVERAGE AUC VALUES COMPUTED UNTIL THE TURNING POINT ACROSS DIFFERENT ARCHITECTURES. LOWER AUC VALUES DENOTE MORE EFFECTIVE EARLY-STAGE DISTANCE REDUCTION.

Model	HSJA	CGBA	CGBA-H	AHA	TEA
ResNet50	53575.41	52130.74	45745.09	44332.55	35133.14
ResNet101	52269.70	49487.56	43865.80	43542.48	34189.94
VGG16	53053.06	53226.27	45261.02	44756.50	35790.23
ViT	44377.75	41097.13	36788.92	37356.25	30337.35

Lower Resolution Performance We evaluate TEA, CGBA, CGBA-H and AHA at two lower input sizes, 128×128 and 64×64 . The Tables V and VI report the median ℓ_2 distance to the source image achieved at fixed query budgets; lower is better. VGG-16 and ViT required standard architectural adjustments at reduced dimensions.

As observable in the results, at lower input resolution sizes, each patch modification distorts a larger fraction of the target image and thus contributes more to the overall ℓ_2 -norm reduction. Consequently, maintaining the adversariality of the image becomes much harder, and TEA therefore terminates earlier than for higher resolutions.

Perceptual Metrics While adversarial examples are generated to trick ML models, it is worth considering their impact on human perception [33], [34]. We report SSIM [35] and FSIM [36] alongside distortion at a fixed budget of 400 queries. As shown in Table VII, TEA achieves high distortion while slightly improving FSIM. A small drop in SSIM is expected, since TEA's perturbations are more structured. Prior image quality assessment (IQA) studies [36], [37] indicate FSIM correlates more strongly with human perception than SSIM, which helps contextualise these differences.

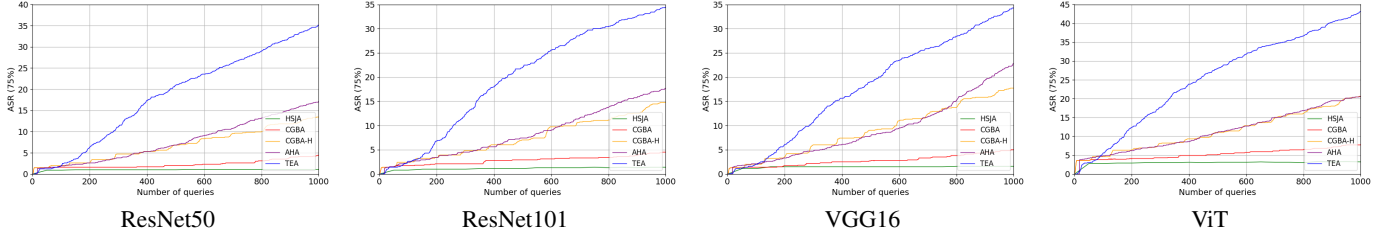


Fig. 5. Comparison of ASR of 75% distance reduction. Higher values indicate that a higher proportion of images reach a distance reduction of 75% sooner.

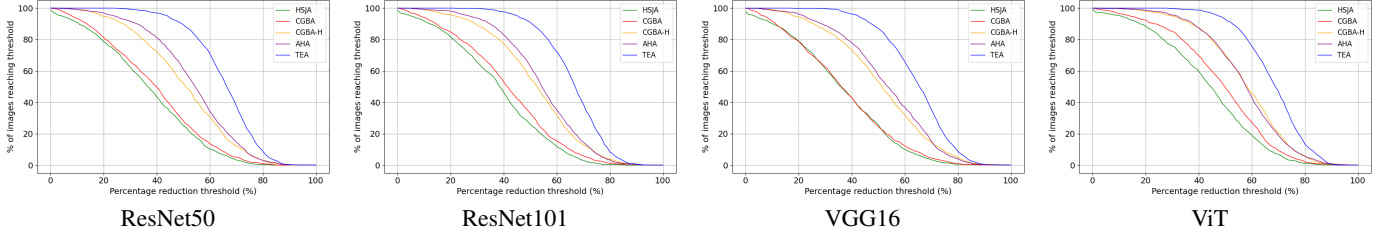


Fig. 6. Cumulative distribution functions (CDFs) of distance reduction at 500 queries. Each curve represents the fraction of image pairs that achieve a given percentage reduction in the ℓ_2 distance, with higher values indicating a more effective reduction method.

TABLE III
EDGE ABALATION IN THE LOW-QUERY REGIME.
PER ARCHITECTURE AND BUDGET WE REPORT MEDIAN ℓ_2 (LOWER IS BETTER), ASR AT 50%, AND ASR AT 75% (HIGHER IS BETTER).

Query	ResNet-50									Query	ResNet-101									
	ℓ_2			ASR@50%			ASR@75%				ℓ_2			ASR@50%			ASR@75%			
	TEA	Half	Inv	TEA	Half	Inv	TEA	Half	Inv		TEA	Half	Inv	TEA	Half	Inv	TEA	Half	Inv	
100	75.1377	87.3465	87.5367	44.0	23.6	22.8	2.0	0.2	1.3	100	74.4637	86.1526	86.8610	44.4	24.1	23.2	2.8	0.3	1.0	
200	61.8307	73.1697	73.3559	70.5	49.7	45.2	6.5	0.7	2.6	200	61.3517	71.7322	72.6071	72.4	53.3	47.3	6.9	0.9	3.1	
300	55.3574	65.0474	66.5448	81.8	67.8	61.8	10.7	3.3	4.4	300	54.9709	63.5007	65.8087	83.9	69.7	62.0	11.8	3.2	4.7	
400	51.8838	60.0257	63.2027	86.0	77.6	69.0	15.6	5.9	6.1	400	51.3084	58.5084	62.4517	87.5	77.6	69.0	17.1	6.7	6.0	
500	49.8877	56.8181	61.6506	87.5	81.8	71.3	19.2	9.5	6.9	500	49.3153	55.3806	60.8018	89.6	82.6	72.2	19.7	9.5	6.5	
VGG16																				
Query	ℓ_2			ASR@50%			ASR@75%			Query	ℓ_2			ASR@50%			ASR@75%			
	TEA	Half	Inv	TEA	Half	Inv	TEA	Half	Inv		TEA	Half	Inv	TEA	Half	Inv	TEA	Half	Inv	
	100	77.4206	90.7514	89.8802	38.1	17.6	20.8	2.0	0.3		0.8	100	67.4874	76.4322	77.6473	57.8	43.4	40.4	5.2	0.9
200	63.7679	75.3909	75.5661	66.3	45.0	40.8	5.8	0.7	2.3	200	56.2801	63.8529	66.0835	80.0	69.8	60.8	11.8	3.6	6.7	
300	57.0986	66.5727	68.5222	78.7	64.8	56.9	10.8	2.9	3.9	300	50.8057	57.2091	60.8559	88.1	82.8	71.0	17.5	7.7	9.7	
400	53.4352	61.0717	65.1434	83.3	74.9	62.9	16.8	7.4	5.0	400	47.9956	53.3073	58.3993	90.6	88.1	74.5	22.9	12.7	12.1	
500	51.4759	57.5518	63.4061	84.7	79.2	66.6	19.5	11.4	6.8	500	46.3913	51.0218	57.2895	92.1	90.6	76.0	26.1	16.2	13.0	

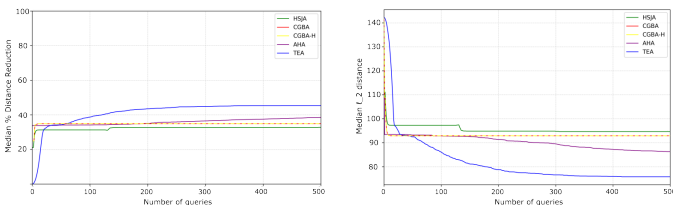


Fig. 7. Comparison on an adversarially trained model. Left: median percentage decrease in ℓ_2 distance against number of queries, with higher values indicating a more effective reduction method. Right: median ℓ_2 distance against number of queries, with lower values indicating a more effective reduction method.

High-Query Performance with CGBA-H refinement.

Our hybrid TEA+CGBA-H strategy consistently matches or surpasses the state-of-the-art. Table VIII lists the median ℓ_2 distances upto 20000 queries. Note that since CGBA-H is

randomness-dependent, it doesn't re-explore when trapped in a narrow decision space and its stability is subject to local decision boundary geometry. Figure 8 illustrates the median percentage reduction in the distance between the images.

Source-Target Similarity Analysis. To examine how the performance of TEA depends on the similarity between source and target images, we group the 1000 source-image pairs by structural similarity. For each pair (x_s, x_t) we compute the SSIM score and sort all pairs by SSIM, partitioning them into ten equally sized bins. Within each bin, and model, we measure the percentage ℓ_2 reduction at a fixed budget of 400 queries. We then average this quantity over all pairs in the same bin and plot the resulting curves (Figure 9). We see that all methods have relatively identical performance variability, with improved performance across structurally similar source-target image pairs. This indicates that structural similarity does not favor TEA over the other methods.

TABLE IV
RANDOMNESS ANALYSIS ACROSS FIVE RUNS: ℓ_2 (MEAN \pm STD).

Budget	ResNet50	ResNet101	VGG16	ViT
50	88.1415 \pm 0.0254	87.0992 \pm 0.0637	90.6675 \pm 0.0553	78.7152 \pm 0.0277
100	75.2155 \pm 0.2338	74.5036 \pm 0.0676	77.2608 \pm 0.1085	67.5654 \pm 0.0652
150	67.3196 \pm 0.2301	66.6368 \pm 0.1022	69.1007 \pm 0.1479	60.6342 \pm 0.1187
200	62.0338 \pm 0.2607	61.3794 \pm 0.1318	63.6530 \pm 0.1896	56.1255 \pm 0.0829
250	58.2941 \pm 0.2458	57.6515 \pm 0.1356	59.7896 \pm 0.2565	53.0414 \pm 0.0537
300	55.5589 \pm 0.1995	54.9321 \pm 0.1397	56.9954 \pm 0.2654	50.8059 \pm 0.0627
400	51.9530 \pm 0.1907	51.3780 \pm 0.1564	53.4018 \pm 0.2513	47.8666 \pm 0.0654
500	49.8352 \pm 0.1522	49.3863 \pm 0.1306	51.3763 \pm 0.2361	46.2528 \pm 0.0899

TABLE V
MEDIAN ℓ_2 DISTANCES AT 128 \times 128.

Query	ResNet50				Query	ResNet101			
	AHA	CGBA	CGBA-H	TEA		AHA	CGBA	CGBA-H	TEA
50	52.812610	56.892204	56.892204	53.891792	50	52.325765	55.829930	55.830184	52.836270
100	49.792591	52.638543	52.610928	44.656296	100	49.256166	51.690833	52.297024	43.908848
150	47.580821	48.751302	48.900604	40.200085	150	47.165379	47.665892	48.747030	39.356266
200	45.816245	47.670539	47.708520	37.588080	200	45.418667	46.499661	48.731472	36.744068
250	44.242092	47.291906	47.416906	35.637354	250	43.904684	45.875023	48.286582	34.803333
300	42.705044	45.310037	45.394565	34.083014	300	43.015997	43.947135	46.251110	33.364790
350	41.704023	45.917060	46.053402	32.915845	350	42.285534	45.637712	48.112825	32.363468
400	40.606535	43.876574	44.083020	31.711626	400	41.279571	43.208419	47.001603	31.200894
Query	VGG16				Query	ViT			
	AHA	CGBA	CGBA-H	TEA		AHA	CGBA	CGBA-H	TEA
50	53.742676	57.595045	57.595044	54.653168	50	49.717520	61.999604	61.999605	51.518260
100	50.687319	53.132007	53.124912	45.101308	100	46.560914	56.845693	56.760291	42.468795
150	48.452131	48.769476	48.688020	40.641963	150	44.133746	51.938031	51.849316	37.765469
200	46.376375	47.648656	47.548296	37.729822	200	42.135314	52.195369	52.190025	34.882641
250	44.719990	46.665404	46.692002	35.775914	250	40.692779	50.410471	50.458582	32.847132
300	43.824315	44.433300	44.557708	34.574623	300	39.469095	47.456320	47.224463	31.225525
350	42.589694	45.370771	45.405220	33.251792	350	38.537397	49.233241	49.101166	30.127403
400	41.597263	43.446274	43.461510	32.151386	400	37.460420	47.532119	47.482755	29.117229

TABLE VI
MEDIAN ℓ_2 DISTANCES AT 64 \times 64.

Query	ResNet50				Query	ResNet101			
	AHA	CGBA	CGBA-H	TEA		AHA	CGBA	CGBA-H	TEA
50	28.562640	31.263057	31.263184	29.709433	50	28.527201	31.240249	31.240327	29.828940
100	26.583674	28.666067	28.734703	25.884418	100	26.545651	28.491136	28.543173	26.137666
150	25.094041	26.041276	26.107465	23.768843	150	25.101155	25.824065	25.971276	23.934921
200	23.449901	24.898503	25.231694	21.971898	200	23.850520	24.798062	25.058821	22.132178
250	22.191710	24.117243	24.478960	20.671545	250	22.805084	23.948980	24.090509	20.863024
Query	VGG16				Query	ViT			
	AHA	CGBA	CGBA-H	TEA		AHA	CGBA	CGBA-H	TEA
50	28.318550	30.844857	30.837613	29.530338	50	30.081730	32.758422	32.758422	31.046581
100	26.390916	28.302722	28.346767	25.606639	100	27.818672	29.806229	29.807765	27.077744
150	24.731502	25.578313	25.651390	23.405260	150	26.072833	26.316862	26.340219	24.609781
200	23.409042	24.719593	24.810609	21.847981	200	24.510567	24.761248	24.786895	22.262164
250	22.453166	23.539063	23.687779	20.527478	250	23.248782	23.717796	23.829428	20.461638

Edge-Density Analysis. To assess how TEA behaves under different levels of structural detail in the source and target images, we perform an edge-density based stratification of the source-target pairs. For each image, we convert it to grayscale, compute Sobel gradients, and form the normalized gradient magnitude $\tilde{g}(p) \in [0, 1]$ for each pixel p . Pixels with

$\tilde{g}(p) > 0.2$ are treated as edge pixels, and the edge density $d(x)$ is defined as the fraction of pixels classified as edges. We collect $d(x_s)$ and $d(x_t)$ for all source-target image pairs and set a global dense/sparse threshold τ_{dense} to be the median density over all 2000 images, yielding $\tau_{\text{dense}} \approx 0.110242$ in our case. Images with $d(x) > \tau_{\text{dense}}$ are labeled *dense*,

TABLE VII
SSIM AND FSIM AT 400 QUERIES ON 1000 SOURCE—TARGET PAIRS.
LOWER ℓ_2 INDICATES SMALLER PERTURBATIONS; HIGHER SSIM/FSIM INDICATES GREATER PERCEPTUAL SIMILARITY TO THE SOURCE IMAGE.

Metric	ResNet50				ResNet101			
	CGBA	CGBA-H	AHA	TEA	CGBA	CGBA-H	AHA	TEA
ℓ_2	85.579	71.479	64.172	51.9530	82.483	68.803	67.051	51.3780
SSIM	0.531765	0.530459	0.231784	0.478806	0.525847	0.528782	0.223511	0.491950
FSIM	0.251337	0.252585	0.232117	0.294672	0.252746	0.251235	0.223831	0.288153
Metric	VGG16				ViT			
	CGBA	CGBA-H	AHA	TEA	CGBA	CGBA-H	AHA	TEA
ℓ_2	89.880	70.559	68.538	53.4018	72.839	61.300	59.857	47.8666
SSIM	0.534783	0.532189	0.231784	0.457879	0.580527	0.582544	0.201767	0.548110
FSIM	0.251129	0.251239	0.232117	0.305919	0.220927	0.220213	0.202171	0.257571

TABLE VIII
MEDIAN ℓ_2 DISTANCES ACROSS DIFFERENT ARCHITECTURES.
HERE, TEA* INDICATES USING TEA UNTIL THE TURNING POINT, AND REFINING FURTHER WITH CGBA-H.

Query	ResNet50					Query	ResNet101				
	HSJA	CGBA	CGBA-H	AHA	TEA*		HSJA	CGBA	CGBA-H	AHA	TEA*
1000	86.800	80.709	58.815	52.069	41.108	1000	86.162	76.005	55.824	51.642	40.090
2500	85.262	69.031	39.701	33.165	29.747	2500	85.314	63.477	38.043	33.259	29.965
5000	83.345	48.703	22.835	18.394	18.338	5000	84.202	41.437	22.470	18.780	18.932
10000	81.623	22.094	10.214	8.597	8.798	10000	82.443	17.623	10.341	9.021	9.864
15000	80.642	10.999	5.908	6.757	5.429	15000	81.873	8.936	6.341	6.937	6.281
20000	79.605	6.594	4.185	6.449	4.011	20000	80.886	5.689	4.507	6.644	4.560
Query	VGG16					Query	ViT				
	HSJA	CGBA	CGBA-H	AHA	TEA*		HSJA	CGBA	CGBA-H	AHA	TEA*
1000	87.451	85.772	56.388	52.361	41.578	1000	79.212	64.516	49.394	49.541	38.482
2500	86.346	74.963	35.686	30.429	27.984	2500	78.739	44.789	32.573	34.762	28.134
5000	85.219	53.869	19.753	16.076	16.050	5000	78.170	25.118	18.566	22.197	18.507
10000	85.219	20.792	8.558	7.456	7.626	10000	77.786	10.319	9.299	11.267	9.416
15000	85.219	9.455	5.306	6.238	4.979	15000	77.087	5.920	5.987	8.180	6.301
20000	85.219	5.687	3.985	6.042	3.823	20000	76.727	4.258	4.635	7.404	4.955

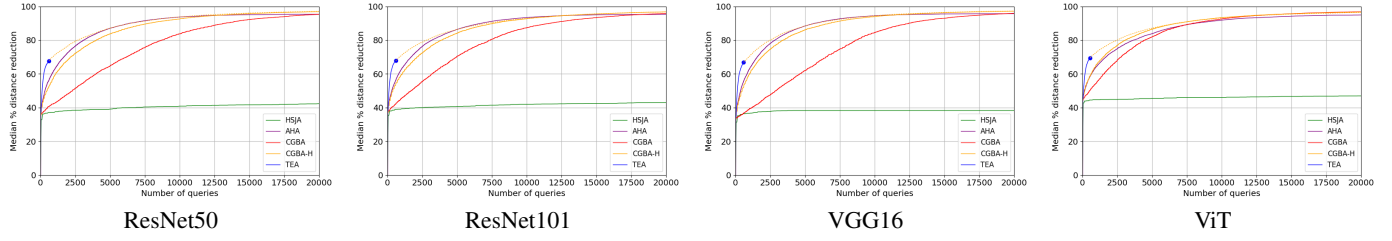


Fig. 8. Comparison of median percentage decrease in ℓ_2 distance across different architectures — higher values indicate a more effective reduction method.

and the rest *sparse*. Each pair (x_s, x_t) is thus assigned to one of four edge-pattern regimes: dense–sparse, dense–dense, sparse–sparse, or sparse–dense. For each regime, and model, we report the average percentage ℓ_2 reduction (in %) at a fixed budget of 400 queries. The resulting curves in Figure 10 show that performance variability is similar across methods, with higher success when moving towards a sparse source image than a dense one, and that TEA maintains a consistent advantage across all regimes.

Zero-Shot CLIP. To assess whether TEA also transfers to more modern vision-language models, we additionally eval-

uate it against a zero-shot CLIP classifier on the ImageNet validation set. We use the ViT-B/32 variant of CLIP [30], [38] in its standard zero-shot configuration. Following the usual protocol, we construct a linear zero-shot head by encoding multiple natural-language templates for each ImageNet class (e.g., “a photo of a {}”, “a close-up photo of a {}.”) with the CLIP text encoder, normalizing and averaging the resulting embeddings to obtain a single prototype per class. Stacking these prototypes yields a fixed weight matrix, and logits are obtained by taking scaled dot products between normalized image features and these class prototypes. Our implementation

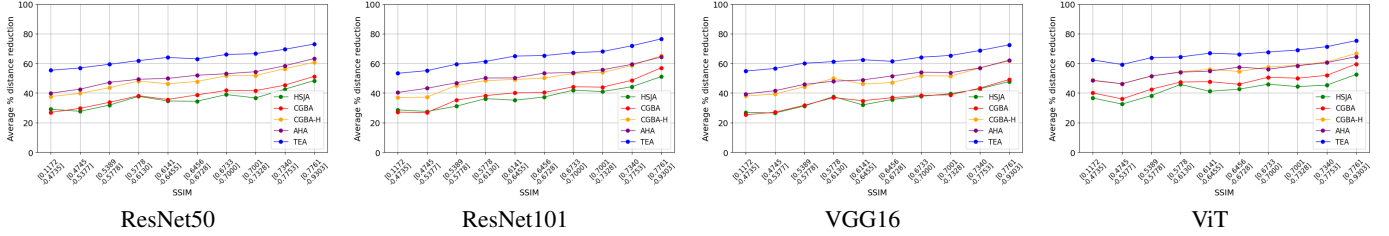


Fig. 9. Effect of source–target structural similarity on attack performance. We group image pairs into ten bins by SSIM and report the average percentage decrease in ℓ_2 distance after 400 queries. All methods benefit similarly from higher structural similarity.

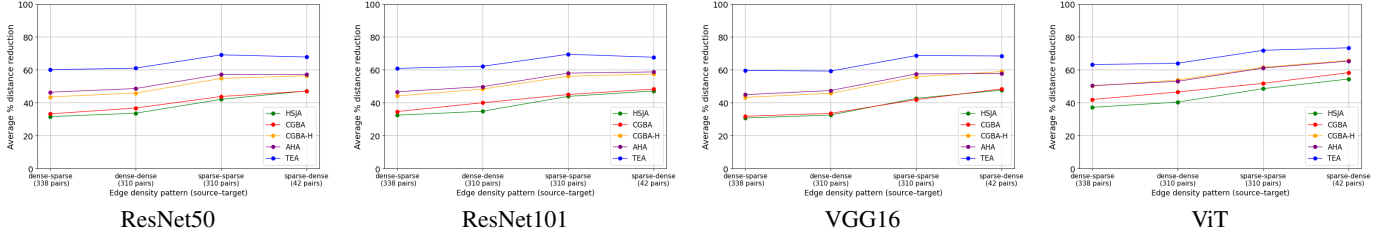


Fig. 10. Effect of source–target edge density on attack performance. Each image is classified as *dense* or *sparse* based on a Sobel edge–density threshold, inducing four edge–pattern regimes (dense–dense, dense–sparse, sparse–dense, sparse–sparse). For each regime, and model, we report the average percentage decrease in ℓ_2 distance after 400 queries, illustrating how performance varies with the edge richness of the source–target pairs.

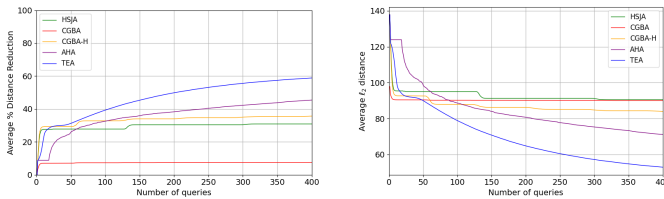


Fig. 11. Comparison on a zero-shot CLIP (ViT-B/32) classifier on ImageNet. Left: average percentage decrease in ℓ_2 distance against number of queries, with higher values indicating a more effective reduction method. Right: average ℓ_2 distance against number of queries, with lower values indicating a more effective reduction method.

relies on the official CLIP PyTorch code-base and its recommended preprocessing.

In Figure 11, we show the average percentage decrease in ℓ_2 distance and the average ℓ_2 distance as a function of the query budget. TEA retains a clear advantage, consistently achieving larger perturbation reductions than the baselines within the same limited query budget, indicating that its strategy remains effective even for modern zero-shot vision-language models.

Other Datasets. To further assess the robustness and generality of TEA beyond ImageNet, we additionally evaluate all tested methods on two standard classification benchmark datasets: CIFAR-100 [39] and the Intel Image Classification dataset [40]. CIFAR-100 contains 100 object categories with lower-resolution images while the Intel dataset consists of six scene categories (e.g., buildings, forest, sea). In both cases, we again attack the four models, ResNet-50, ResNet-101, VGG-16, and ViT, and measure performance in terms of the relative ℓ_2 -distance reduction between the source and target images. Figures 12 and 13 report the average ℓ_2 -distance reduction at a fixed low-query budget of 400 across all four

models. Consistent with our results on the ImageNet dataset, TEA achieves larger perturbation reductions on both datasets, indicating that its edge-aware strategy remains effective across diverse data distributions and resolutions.

V. CONCLUSION

In this work, we introduced *TEA*, a targeted, hard-label, black-box adversarial attack that leverages edge information from a target image to efficiently produce adversarial examples perceptually closer to a source image in low-query settings. TEA initially employs a global search that preserves prominent edge structures across the target image, subsequently refining the perturbations via patch-wise updates. Empirical results demonstrate that TEA significantly reduces the ℓ_2 distance between adversarial and source images, requiring over 70% fewer queries compared to current state-of-the-art methods. In addition, it also achieves reduced AUC and high ASR scores, indicating a consistently rapid reduction in distance to the source image across different models.

Limitations. TEA is specifically designed for the targeted, hard-label, low-query black-box setting, and its main advantage lies in rapidly improving performance under tight query budgets. When TEA is used merely as an initialization and followed by stronger high-query attacks in regimes where many queries are available, we observe that the final performance is comparable to that of the underlying state-of-the-art methods, rather than strictly better. In addition, while TEA preserves global edge structure and achieves low ℓ_2 distances, the patch-wise updates can still introduce localized artifacts that are visible to human observers. This limitation is shared with other norm-bounded attacks in general, but in TEA the patch-based nature of the perturbations can make these local changes particularly noticeable.

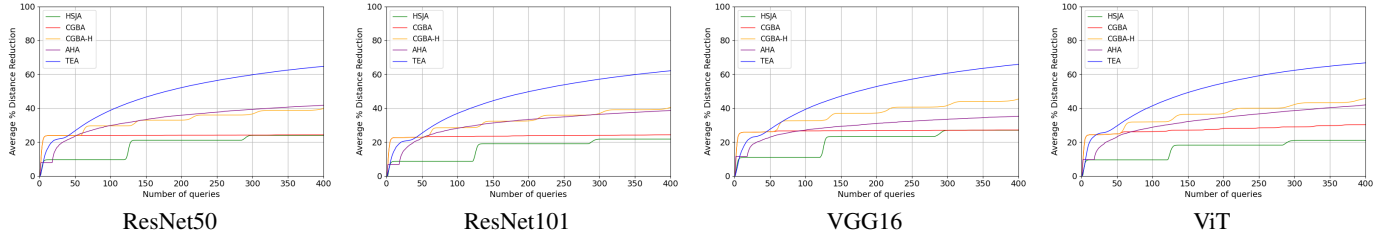


Fig. 12. Average ℓ_2 distance reduction across different architectures in a low-query regime on the CIFAR-100 dataset.

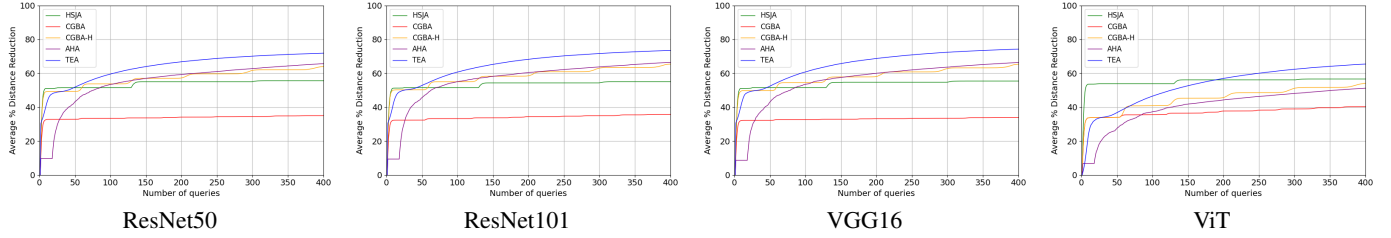


Fig. 13. Average ℓ_2 distance reduction across different architectures in a low-query regime on the Intel Image Classification dataset.

Future Work. Several extensions could enhance TEA: (a) substituting edge information with other features such as textures, color distributions, or high-frequency components; (b) training a surrogate model based on query data already collected to guide subsequent perturbations and (c) developing defense mechanisms capable of mitigating attacks based on structure-preserving perturbations.

CODE AVAILABILITY

Our code is available at the following URL: <https://github.com/mdppml/TEA>.

CODE OF ETHICS AND BROADER IMPACT STATEMENT

We evaluate TEA exclusively on the publicly available ImageNet-1K validation set, which is distributed for non-commercial research and educational use under the ImageNet access agreement. The dataset contains no personally identifiable information, and was used in accordance with the license terms. As TEA reduces the number of required queries for targeted hard-label attacks in a low-query setting, it could be leveraged to more rapidly craft adversarial inputs against commercial or safety-critical vision systems. We encourage practitioners to adopt defense mechanisms that go beyond detecting frequency-based perturbations, explicitly incorporating checks for edge-informed distortions, and defenses attuned to other structural features, to guard against similar attacks.

LLM USAGE CONSIDERATIONS

LLMs were used for editorial purposes in this manuscript, and all outputs were inspected by the authors to ensure accuracy and originality. All technical ideas, experiments, analyses, and citations were conceived, implemented, and validated by the authors.

ACKNOWLEDGMENTS

This research was supported by the German Federal Ministry of Education and Research (BMBF) under project number 01ZZ2010 and partially funded through grant 01ZZ2316D (PrivateAIM). The authors acknowledge the usage of the Training Center for Machine Learning (TCML) cluster at the University of Tübingen.

REFERENCES

- [1] M. Bojarski, D. Del Testa, D. Dworakowski, B. Firner, B. Flepp, P. Goyal, L. D. Jackel, M. Monfort, U. Muller, J. Zhang *et al.*, “End to end learning for self-driving cars,” *arXiv preprint arXiv:1604.07316*, 2016.
- [2] C. Chen, A. Seff, A. Kornhauser, and J. Xiao, “Deepdriving: Learning affordance for direct perception in autonomous driving,” in *Proceedings of the IEEE international conference on computer vision*, 2015, pp. 2722–2730.
- [3] A. Esteva, B. Kuprel, R. A. Novoa, J. Ko, S. M. Swetter, H. M. Blau, and S. Thrun, “Dermatologist-level classification of skin cancer with deep neural networks,” *nature*, vol. 542, no. 7639, pp. 115–118, 2017.
- [4] K. He, X. Zhang, S. Ren, and J. Sun, “Deep residual learning for image recognition,” in *Proceedings of the IEEE conference on computer vision and pattern recognition*, 2016, pp. 770–778.
- [5] I. J. Goodfellow, J. Shlens, and C. Szegedy, “Explaining and harnessing adversarial examples,” *arXiv preprint arXiv:1412.6572*, 2014.
- [6] C. Szegedy, W. Zaremba, I. Sutskever, J. Bruna, D. Erhan, I. Goodfellow, and R. Fergus, “Intriguing properties of neural networks,” *arXiv preprint arXiv:1312.6199*, 2013.
- [7] A. Ilyas, L. Engstrom, A. Athalye, and J. Lin, “Black-box adversarial attacks with limited queries and information,” in *International conference on machine learning*. PMLR, 2018, pp. 2137–2146.
- [8] M. Cheng, S. Singh, P. Chen, P.-Y. Chen, S. Liu, and C.-J. Hsieh, “Sign-opt: A query-efficient hard-label adversarial attack,” *arXiv preprint arXiv:1909.10773*, 2019.
- [9] S. Cheng, Y. Dong, T. Pang, H. Su, and J. Zhu, “Improving black-box adversarial attacks with a transfer-based prior,” *Advances in neural information processing systems*, vol. 32, 2019.
- [10] V. Q. Vo, E. Abbasnejad, and D. C. Ranasinghe, “Ramboattack: A robust query efficient deep neural network decision exploit,” *arXiv preprint arXiv:2112.05282*, 2021.
- [11] P.-Y. Chen, H. Zhang, Y. Sharma, J. Yi, and C.-J. Hsieh, “Zoo: Zeroth order optimization based black-box attacks to deep neural networks without training substitute models,” in *Proceedings of the 10th ACM workshop on artificial intelligence and security*, 2017, pp. 15–26.

[12] M. Cheng, T. Le, P.-Y. Chen, H. Zhang, J. Yi, and C.-J. Hsieh, “Query-efficient hard-label black-box attack: An optimization-based approach,” in *International Conference on Learning Representations*, 2018.

[13] W. Brendel, J. Rauber, and M. Bethge, “Decision-based adversarial attacks: Reliable attacks against black-box machine learning models,” *arXiv preprint arXiv:1712.04248*, 2017.

[14] T. Brunner, F. Diehl, M. T. Le, and A. Knoll, “Guessing smart: Biased sampling for efficient black-box adversarial attacks,” in *Proceedings of the IEEE/CVF International Conference on Computer Vision*, 2019, pp. 4958–4966.

[15] T. Maho, T. Furun, and E. Le Merrer, “Surfree: a fast surrogate-free black-box attack,” in *Proceedings of the IEEE/CVF conference on computer vision and pattern recognition*, 2016, pp. 770–778.

[16] F. Suya, J. Chi, D. Evans, and Y. Tian, “Hybrid batch attacks: Finding black-box adversarial examples with limited queries,” in *29th USENIX security symposium (USENIX Security 20)*, 2020, pp. 1327–1344.

[17] J. Chen, M. I. Jordan, and M. J. Wainwright, “Hopskipjumpattack: A query-efficient decision-based attack,” in *2020 ieee symposium on security and privacy (sp)*. IEEE, 2020, pp. 1277–1294.

[18] H. Li, X. Xu, X. Zhang, S. Yang, and B. Li, “Qeba: Query-efficient boundary-based blackbox attack,” in *Proceedings of the IEEE/CVF conference on computer vision and pattern recognition*, 2020, pp. 1221–1230.

[19] Y. Liu, S.-M. Moosavi-Dezfooli, and P. Frossard, “A geometry-inspired decision-based attack,” in *Proceedings of the IEEE/CVF International Conference on Computer Vision*, 2019, pp. 4890–4898.

[20] C. Ma, X. Guo, L. Chen, J.-H. Yong, and Y. Wang, “Finding optimal tangent points for reducing distortions of hard-label attacks,” *Advances in Neural Information Processing Systems*, vol. 34, pp. 19288–19300, 2021.

[21] M. F. Reza, A. Rahmati, T. Wu, and H. Dai, “Cgba: Curvature-aware geometric black-box attack,” in *Proceedings of the IEEE/CVF international conference on computer vision*, 2023, pp. 124–133.

[22] Y. Tashiro, Y. Song, and S. Ermon, “Diversity can be transferred: Output diversification for white-and black-box attacks,” *Advances in neural information processing systems*, vol. 33, pp. 4536–4548, 2020.

[23] X. Wang, Z. Zhang, K. Tong, D. Gong, K. He, Z. Li, and W. Liu, “Triangle attack: A query-efficient decision-based adversarial attack,” in *European conference on computer vision*. Springer, 2022, pp. 156–174.

[24] I. Sobel, “Neighborhood coding of binary images for fast contour following and general binary array processing,” *Computer graphics and image processing*, vol. 8, no. 1, pp. 127–135, 1978.

[25] R. Bassett, M. Graves, and P. Reilly, “Color and edge-aware adversarial image perturbations,” *arXiv preprint arXiv:2008.12454*, 2020.

[26] M. D. Zeiler and R. Fergus, “Visualizing and understanding convolutional networks,” in *Computer Vision-ECCV 2014: 13th European Conference, Zurich, Switzerland, September 6-12, 2014, Proceedings, Part I 13*. Springer, 2014, pp. 818–833.

[27] R. Geirhos, P. Rubisch, C. Michaelis, M. Bethge, F. A. Wichmann, and W. Brendel, “Imagenet-trained cnns are biased towards texture; increasing shape bias improves accuracy and robustness,” in *International conference on learning representations*, 2018.

[28] J. Deng, W. Dong, R. Socher, L.-J. Li, K. Li, and L. Fei-Fei, “Imagenet: A large-scale hierarchical image database,” in *2009 IEEE conference on computer vision and pattern recognition*. Ieee, 2009, pp. 248–255.

[29] K. Simonyan and A. Zisserman, “Very deep convolutional networks for large-scale image recognition,” *arXiv preprint arXiv:1409.1556*, 2014.

[30] A. Dosovitskiy, L. Beyer, A. Kolesnikov, D. Weissenborn, X. Zhai, T. Unterthiner, M. Dehghani, M. Minderer, G. Heigold, S. Gelly *et al.*, “An image is worth 16x16 words: Transformers for image recognition at scale,” *arXiv preprint arXiv:2010.11929*, 2020.

[31] L. Engstrom, A. Ilyas, H. Salman, S. Santurkar, and D. Tsipras, “Robustness (python library),” 2019. [Online]. Available: <https://github.com/MadryLab/robustness>

[32] J. Li, R. Ji, P. Chen, B. Zhang, X. Hong, R. Zhang, S. Li, J. Li, F. Huang, S. Ren, and Y. Sun, JiWu, “Aha! adaptive history-driven attack for decision-based black-box models,” in *Proceedings of the IEEE/CVF International Conference on Computer Vision*, 2021, pp. 16168–16177.

[33] N. Carlini and D. Wagner, “Towards evaluating the robustness of neural networks,” in *2017 ieee symposium on security and privacy (sp)*. Ieee, 2017, pp. 39–57.

[34] Q.-A. Fu, Y. Dong, H. Su, J. Zhu, and C. Zhang, “[AutoDA]: Automated decision-based iterative adversarial attacks,” in *31st USENIX Security Symposium (USENIX Security 22)*, 2022, pp. 3557–3574.

[35] Z. Wang, A. C. Bovik, H. R. Sheikh, and E. P. Simoncelli, “Image quality assessment: from error visibility to structural similarity,” *IEEE transactions on image processing*, vol. 13, no. 4, pp. 600–612, 2004.

[36] L. Zhang, L. Zhang, X. Mou, and D. Zhang, “Fsim: A feature similarity index for image quality assessment,” *IEEE transactions on Image Processing*, vol. 20, no. 8, pp. 2378–2386, 2011.

[37] S. A. Fezza, Y. Bakhti, W. Hamidouche, and O. Déforges, “Perceptual evaluation of adversarial attacks for cnn-based image classification,” in *2019 eleventh international conference on quality of multimedia experience (QoMEX)*. IEEE, 2019, pp. 1–6.

[38] A. Radford, J. W. Kim, C. Hallacy, A. Ramesh, G. Goh, S. Agarwal, G. Sastry, A. Askell, P. Mishkin, J. Clark *et al.*, “Learning transferable visual models from natural language supervision,” in *International conference on machine learning*. PMLR, 2021, pp. 8748–8763.

[39] A. Krizhevsky, “Learning multiple layers of features from tiny images,” Technical report, University of Toronto, Toronto, ON, Canada, 2009.

[40] Intel and Analytics Vidhya, “Intel image classification (scene classification challenge),” <https://www.kaggle.com/datasets/puneet6060/intel-image-classification>, 2018, originally released as the Intel Scene Classification Challenge on Analytics Vidhya.